

Enhancing the hyperbolic bandwidth in two-dimensional materials via atomic orbital engineering

Shuting Hou, Xikui Ma, Chao Ding, Yuezeng Du, and Mingwen Zhao[✉]

School of Physics, Shandong University, Jinan 250100, China



(Received 24 March 2024; revised 7 July 2024; accepted 15 July 2024; published 2 August 2024)

The emergence of two-dimensional (2D) hyperbolic materials, characterized by opposite-sign optical conductivities along two orthogonal axes within a specific band (known as the hyperbolic region), opens an avenue for optical device engineering. Broadening the hyperbolic region is essential for cutting-edge photonic applications. In this study, based on a correlation between the hyperbolic region and anisotropic electronic structures, we propose a strategic framework for identifying 2D natural hyperbolic materials (NHMs) with broadband hyperbolicity. Using this framework, we engineered a 2D lattice incorporating *p* and *d* orbitals, and discovered a series of 2D NHMs, *MYZ* (*M* = Co, Pd, Ru, Rh; *Y* = S, Se, Te; and *Z* = Cl, Br, I). These materials exhibit broadband hyperbolicity that extends from the near-infrared to the visible-light spectrum. We have confirmed the directional propagation of surface plasmon polaritons on these 2D materials based on Maxwell's equations. Our findings pave the way for future exploration and practical deployment of 2D NHMs in advanced technological applications.

DOI: 10.1103/PhysRevApplied.22.024005

I. INTRODUCTION

Surface plasmon polaritons (SPPs), which occur at the interface between a metallic material and a dielectric medium, represent collective oscillations of the free electrons in a metallic medium coupled with an electromagnetic field, enabling subwavelength waveguiding and substantially amplifying light-matter interactions [1–4]. The dispersion relation of SPPs is distinct from that of light in a dielectric medium or plasmons in metals alone. Materials that support SPPs with hyperbolic isofrequency contours (IFCs) within a specific band (hyperbolic region) are classified as hyperbolic materials. This unique hyperbolic dispersion leads to exceptional optical phenomena, such as all-angle negative refraction [5,6]. Initially achieved in artificially engineered metamaterials, hyperbolic IFCs have opened the door to a wide range of applications, such as superresolution imaging [7,8], enhanced light-matter interactions [2,3,9], near-field radiative heat transfer [10,11], plasmonics, surface-enhanced spectroscopy [12,13], and advancements in terahertz devices [14,15], as well as photonic band gap engineering [16–18].

The emergence of two-dimensional (2D) materials has revolutionized the search for hyperbolic materials, driven by their distinctive electronic structures and unique plasmonic characteristics. These materials present a low damping rate, high confinement, and exceptional tenability [19–22]. Unlike engineered metasurfaces, 2D natural

hyperbolic materials (NHMs) benefit from their atomic-scale periodicity, which facilitates the production of large wave vectors without the complexity of intricate surface patterning [23]. The hyperbolic IFC fosters the propagation of large wave-vector waves, leading to an increased photonic density of states [24,25]. Particularly intriguing is the ability of 2D hyperbolic materials to guide directional SPPs confined to subwavelength dimensions, which enhance light-matter interaction at the nanoscale. These distinctive properties have profound implications for a diverse array of applications, spanning sensing, nonlinear optics, and integrated photonic circuits [26–28].

Several 2D materials such as black phosphorus [29,30], WTe₂ [31,32], and α -MoO₃ [33,34] have been identified, either theoretically or experimentally, as NHMs. The hyperbolic behavior observed in these materials is primarily ascribed to their highly anisotropic electronic structures. However, a comprehensive understanding of the connection between the hyperbolic region and these electronic structures is not fully established. Enhancing the hyperbolic bandwidth of 2D materials to satisfy the exacting demands of functional devices remains an intricate and demanding endeavor.

In this study, we set up a direct connection between the hyperbolic region and the anisotropic electronic structure of 2D materials, providing a foundational principle for the engineering of the hyperbolic region in 2D NHMs. We construct a 2D lattice model of *p* and *d* orbitals, which exhibits a pronounced anisotropic electronic structure and significant hyperbolic

*Contact author: zmw@sdu.edu.cn

characteristics stemming from anisotropic orbital ordering. Utilizing this model, we identify a series of 2D NHMs, denoted as *MYZ* (*M*=Co, Pd, Ru, Rh; *Y*=S, Se, Te; and *Z*=Cl, Br, I), that display broadband hyperbolicity through first-principles calculations. The hyperbolic dispersion in these materials extends from the near-infrared to the visible-light spectrum. Additionally, we confirm the directional propagation of SPPs on these 2D materials by applying Maxwell's equations. Our findings offer a promising platform for both the investigation and practical deployment of 2D NHMs.

II. METHOD AND COMPUTATIONAL DETAILS

First-principles calculations are performed using the Vienna *ab initio* simulation package (VASP) [35] in combination with the grid-based projector-augmented wave (GPAW) code [36,37]. Density-functional theory (DFT) with the PAW method [38] is employed to account for ion-electron interactions. The Perdew, Burke, and Ernzerhof generalized gradient approximation exchange-correlation functional [39] is utilized to ensure self-consistency. Plane waves with an energy cutoff of 500 eV are employed to expand the Kohn-Sham wave function. To eliminate interactions between neighboring images, we introduce a vacuum space with a thickness of 30 Å along the *z* direction. Structural relaxation and electronic properties calculations are performed using a $7 \times 11 \times 1$ *k*-points mesh and an energy convergence criterion of 10^{-6} eV is set. Atomic coordinates and lattice vectors are fully relaxed until the Hellmann-Feynman forces a threshold of 0.01 eV/Å, without any symmetry constraints. These computational settings effectively converge to determine optimized lattice parameters and electronic properties of the investigated 2D materials.

III. RESULTS AND DISCUSSION

A. Theory for hyperbolicity in 2D materials

1. 2D optical conductivity model

We begin with a minimal model for the optical conductivity tensor for an anisotropic medium:

$$\sigma = \begin{pmatrix} \sigma_{xx} & 0 \\ 0 & \sigma_{yy} \end{pmatrix}. \quad (1)$$

Within the limits of homogeneity and local response, the optical conductivity tensor becomes a function of frequency ω , no longer dependent on the wavevector \mathbf{q} [40,41]. They can be evaluated using the following expression:

$$\begin{aligned} \sigma_{jj}(\omega) &= \sigma_{jj}^{\text{intra}}(\omega) + \sigma_{jj}^{\text{inter}}(\omega) \\ &= \frac{i}{(\omega + i\gamma)} \sum_{k,l} \left(\frac{\partial E_{k,l}}{\partial k_j} \right)^2 \left(-\frac{\partial f}{\partial E_{k,l}} \right) \end{aligned}$$

$$\begin{aligned} &+ i \sum_{k,l \neq l'} \frac{f(E_{k,l'}) - f(E_{k,l})}{E_{k,l'} - E_{k,l}} \\ &\times \frac{|\langle \mathbf{k}, l | \hat{v}_j | \mathbf{k}, l' \rangle|^2}{(E_{k,l'} - E_{k,l}) - (\omega + i\eta)}, \quad j = x, y. \quad (2) \end{aligned}$$

The first and second terms denote the contributions stemming from intraband and interband transitions, as described by the Drude model [42] and the Kubo formalism [43], respectively. $E_{k,l}$ and $|\mathbf{k}, l\rangle$ denote the eigenvalue and eigenvector of the state of band *l* at \mathbf{k} point, $\hat{v}_j = \partial/\partial k_j$ represents the velocity operator, $f(E_{k,l})$ is the Fermi-Dirac distribution function, and γ and η are the damping rates of the intraband transition and interband transition, respectively.

At $T=0$ K, $-\partial f / \partial E_{k,l}$ can be replaced by $\delta(E_{k,l} - E_F)$ according to the Sommerfeld expansion [44,45], where E_F is the Fermi energy, and the contribution of intraband transitions to optical conductivity simplifies to

$$\sigma_{jj}^{\text{intra}}(\omega) = \frac{i}{\pi} \frac{D_{jj}}{(\omega + i\gamma)}, \quad (3)$$

with $D_{jj} = \pi \rho(E_F) \bar{v}_j^2$. $\rho(E_F) = \sum_{k,l} \delta(E_{k,l} - E_F)$ is the electron density of states at the Fermi level. \bar{v}_j^2 is the averaged square of Fermi velocity along the *j* direction, defined by $\bar{v}_j^2 = (1/(2\pi)^2) \sum_l g_l v_j^2(\mathbf{k}) \delta(E_{k,l} - E_F) d^2\mathbf{k} / \rho(E_F)$ [46]. Here, $v_j = \partial E_{k,l} / \partial k_j$ represents the electron velocity along the *j* direction and g_l denotes the degeneracy of band *l*.

Taking into account the electron transition between two bands, *l*, *l'* $\in (1, 2)$, that predominate in the contribution to optical conductivity within a specific frequency range, and presuming that the peak values of $|\langle \mathbf{k}, 1 | \hat{v}_j | \mathbf{k}, 2 \rangle|^2$ are focused in a distinct region of \mathbf{k} space characterized by the transition energy of $E_{k,2} - E_{k,1} = \omega_b$, the contribution of interband transitions can be distilled to a simpler form:

$$\sigma_{jj}^{\text{inter}}(\omega) \approx \frac{i}{\pi} \frac{S_{jj} \omega}{\omega^2 - \omega_b^2 + i\eta\omega}, \quad (4)$$

with

$$S_{jj} = 2\pi \sum_{\mathbf{k}} \frac{f(E_{k,1}) - f(E_{k,2})}{E_{k,2} - E_{k,1}} \times |\langle \mathbf{k}, 1 | \hat{v}_j | \mathbf{k}, 2 \rangle|^2.$$

Thus, the total optical conductivity, resulting from both interband and intraband transitions, can be expressed as

$$\sigma_{jj}(\omega) \approx \frac{i}{\pi} \frac{D_{jj}}{(\omega + i\gamma)} + \frac{i}{\pi} \frac{S_{jj} \omega}{\omega^2 - \omega_b^2 + i\eta\omega}. \quad (5)$$

This expression has garnered extensive use in deciphering experimental results [47]. The correlation between electronic structures and the two parameters established in this

study offers a compelling strategy for modulating optical conductivity in 2D materials.

2. Hyperbolic region in 2D materials

We then consider the eigenmodes of SPPs confined within a 2D material (x - y plane) characterized by $e^{i(q_x x + q_y y)} e^{-p z}$ (for $z > 0$) and $e^{i(q_x x + q_y y)} e^{p z}$ (for $z < 0$). The dispersion relations of the SPPs are characterized by the following expression [29,48]:

$$(q_x^2 - k_0^2)\sigma_{xx} + (q_y^2 - k_0^2)\sigma_{yy} = 2ip\omega(\varepsilon_0 + \mu_0\sigma_{xx}\sigma_{yy}/4). \quad (6)$$

In this expression, ε_0 , μ_0 , and $k_0 = \omega/\sqrt{\varepsilon_0\mu_0}$ represent the permittivity, permeability, and wave number in vacuum, $p = \sqrt{q_x^2 + q_y^2 - k_0^2}$. For scenarios with low damping,

$\text{Im}\sigma \gg \text{Re}\sigma$, Eq. (6) reduces to

$$(\tilde{q}_x^2 - 1)/\text{Im}\sigma_{yy} + (\tilde{q}_y^2 - 1)/\text{Im}\sigma_{xx} = \kappa(\tilde{q}_x^2 + \tilde{q}_y^2 - 1)^{1/2}, \quad (7)$$

with $\tilde{q}_x = q_x/k_0$, $\tilde{q}_y = q_y/k_0$, and $\kappa = (2\varepsilon_0/(\mu_0 \text{Im}\sigma_{xx} \times \text{Im}\sigma_{yy}) - 1/2) \times (\varepsilon_0/\mu_0)^{-1/2}$. Notably, in the frequency region of $\text{Im}\sigma_{xx} \times \text{Im}\sigma_{yy} < 0$ (hyperbolic region), Eq. (7) leads to hyperbolicalike IFCs, as illustrated in Figs. 1(a) and 1(b). Furthermore, in the limit of $|\tilde{q}_x| \gg 1$ and $|\tilde{q}_y| \gg 1$, there are two asymptotic lines given by $\tilde{q}_x^2/\text{Im}\sigma_{yy} + \tilde{q}_y^2/\text{Im}\sigma_{xx} = 0$. This observation implies that the direction of propagation for SPP beams, which is determined by the group velocity normal to the contour line, can be characterized by an angle of $\varphi = \pm\tan^{-1}|\text{Im}\sigma_{yy}/\text{Im}\sigma_{xx}|^{1/2}$ relative to the x direction.

In Figs. 1(c) and 1(d), the relationship between the hyperbolic region and the zero crossing points ($\omega_{0,j}$) of optical conductivity, as defined by Eq. (5), is depicted for

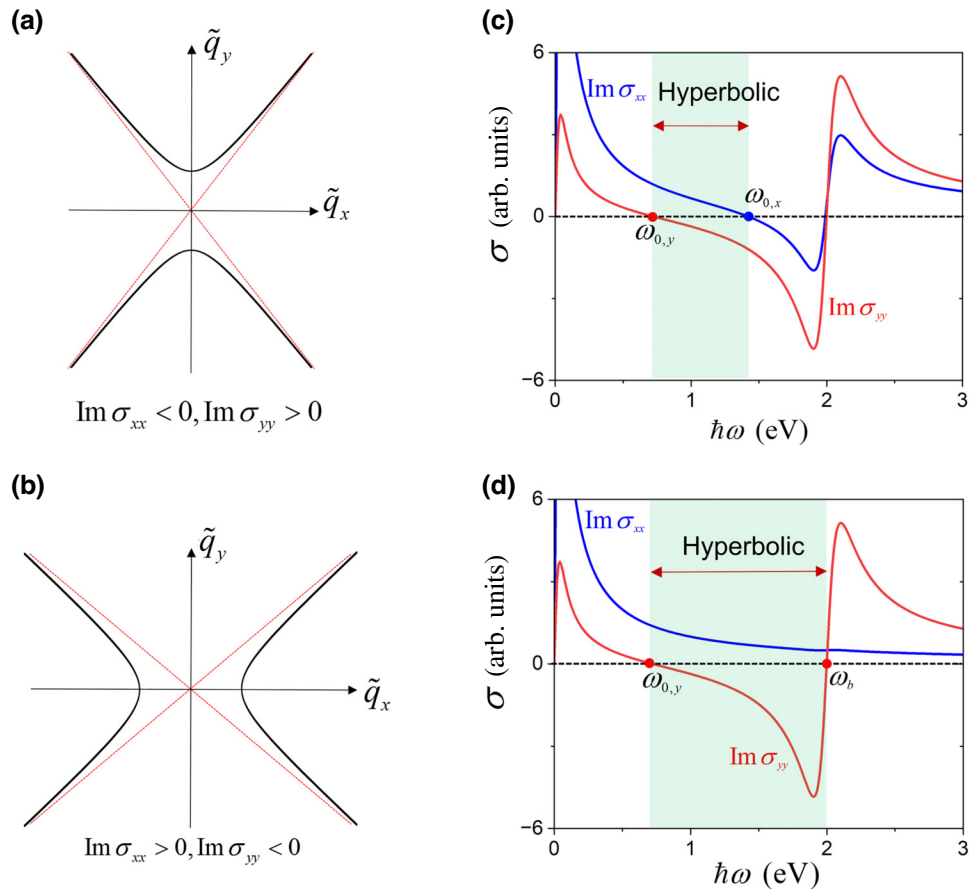


FIG. 1. Schematic representations of IFCs and hyperbolicity. Diagrams of hyperbolic IFCs given by Eq. (7) with (a) $\text{Im}\sigma_{xx} < 0$ and $\text{Im}\sigma_{yy} > 0$ and (b) $\text{Im}\sigma_{xx} > 0$ and $\text{Im}\sigma_{yy} < 0$. The red dotted lines indicate the asymptotic lines of the dispersion relations. The relationship between the hyperbolic region and the zero crossing points ($\omega_{0,j}$) of optical conductivity given by Eq. (5) for (c) $D_{xx} = S_{xx} = 1$, $D_{yy} = 0.1$, $S_{yy} = 1$ and (d) $D_{xx} = 1$, $S_{xx} = 0.01$, $D_{yy} = 0.1$, $S_{yy} = 1$. The damping rates for the intraband transitions and interband transitions are set to $\gamma = 0.01$ eV and $\eta = 0.2$ eV, respectively. The interband transition energy is set to $\omega_b = 2.0$ eV.

two distinct scenarios. In Fig. 1(c), the optical conductivity in the y direction is primarily influenced by interband transitions, whereas both the intraband and interband transitions have comparable impacts on optical conductivity in the x direction. Figure 1(d) highlights the predominance of intraband transitions affecting the optical conductivity in the x direction, while the interband transitions dominate the optical conductivity in the y direction.

Neglecting damping ($\gamma = \eta = 0$), the zero crossing points ($\omega_{0,j}$) of Eq. (5) satisfy

$$\omega_{0,j} = \frac{\omega_b}{\sqrt{1 + S_{jj}/D_{jj}}}. \quad (8)$$

It becomes evident that a larger disparity between S_{xx}/D_{xx} and S_{yy}/D_{yy} results in a broader hyperbolic region. Notably, $S_{jj}/D_{jj} \propto |\langle \mathbf{k}, 1 | \hat{v}_j | \mathbf{k}, 2 \rangle|^2 / \bar{v}_j^2$. The anisotropy of \bar{v}_j^2 is determined by the distribution of Fermi velocity around the Fermi contour, while $|\langle \mathbf{k}, 1 | \hat{v}_j | \mathbf{k}, 2 \rangle|^2$ is

related to the symmetries of $|\mathbf{k}, 1\rangle$ and $|\mathbf{k}, 2\rangle$. The connection between the hyperbolic region and electronic structures presents a viable strategy for engineering of 2D hyperbolic materials. Intuitively, a Fermi contour with pronounced anisotropy that gives rise to a significant difference between \bar{v}_x^2 and \bar{v}_y^2 is conducive to the emergence of a broadband hyperbolicity.

B. A tight-binding model for an anisotropic p - d lattice

To design a highly anisotropic electronic band structure, we employed $d_{x^2-y^2}$ and p_x orbitals, and placed them alternately in a 2D rectangular lattice, as depicted in Fig. 2(a). Notably, this model exhibits significant anisotropic orbital ordering due to the anisotropic p_x orbitals separated by $d_{x^2-y^2}$ orbitals. The electron hopping between adjacent sites along the x direction is characterized by t , while the next-nearest hoppings are characterized by t' and t'' , as illustrated in Fig. 2(a). The on-site energy difference between the $d_{x^2-y^2}$ and p_x orbitals is denoted by Δ . Notably, electron hopping along the y direction between

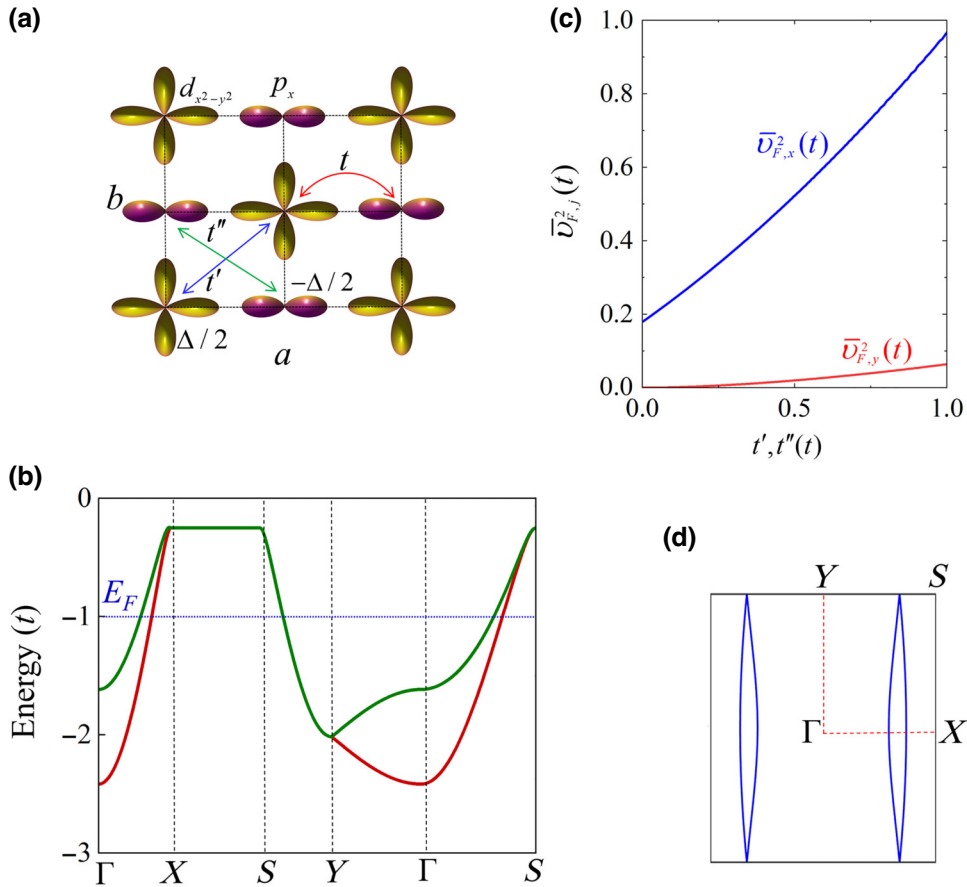


FIG. 2. Tight-binding model for the 2D lattice of $d_{x^2-y^2}$ and p_x orbitals. (a) Schematic representation of orbital arrangement and hopping between them. (b) Tight-binding band structure with $t' = t'' = 0.1t$ and $\Delta = t$. The dotted line represents the position of the Fermi level. (c) The averaged square of Fermi velocity ($\bar{v}_{F,j}^2$) along the x and y directions with respect to the tight-binding parameters. (d) The contours of the Fermi surface. The rectangle indicates the Brillouin zone characterized by the high-symmetry points: $\Gamma(0,0)$, $X(\pi/a, 0)$, $Y(0, \pi/b)$, and $S(\pi/a, \pi/b)$.

adjacent sites is prohibited, owing to the orthogonality between $d_{x^2-y^2}$ and p_x along this direction [49]. This leads to a tight-binding (TB) Hamiltonian as follows:

$$H_{\text{TB}}(\mathbf{k}) = \begin{bmatrix} \Delta/2 & f_{12} & f_{13} & 0 \\ f_{12} & -\Delta/2 & 0 & f_{24} \\ f_{13} & 0 & \Delta/2 & f_{12} \\ 0 & f_{24} & f_{12} & -\Delta/2 \end{bmatrix}, \quad (9)$$

with $f_{12}(\mathbf{k}) = 2t \cos(k_x a/2)$, $f_{13}(\mathbf{k}) = 2t' [\cos(k_x a/2 + k_y b/2) + \cos(k_x a/2 - k_y b/2)]$, and $f_{24}(\mathbf{k}) = 2t'' [\cos(-k_x a/2 + k_y b/2) + \cos(k_x a/2 + k_y b/2)]$. Diagonalizing the TB Hamiltonian, we can get the electronic band structure, as depicted in Fig. 2(b). In the Γ - X direction, which corresponds to the x direction, we observe two dispersive bands, distinguished by their high electron velocities. Considering the correlation between Drude weight D_{jj} and electron velocity \bar{v}_j^2 , this results in a high electron optical conductivity along the x direction. In the Γ - Y direction, however, the bands are rather flat, indicating low electron velocities and thus low optical conductivity along the y direction. This phenomenon can be attributed to the prohibited p - d electron hopping along this direction. The anisotropy of the electronic band structure is more evident from the shape of Fermi contours. Setting the Fermi level to the position that crosses the dispersive bands with $E_F = -t$, we obtain two slender-olive-like Fermi contours, as depicted in Fig. 2(d). Because the direction of Fermi velocity is perpendicular to

the Fermi contour, such a slender-olive-like Fermi contour results in a larger $\bar{v}_{F,x}^2$ than $\bar{v}_{F,y}^2$, as illustrated in Fig. 2(c). Although this TB mode does not include the contribution of interband transition to optical conductivity, the large difference between $\bar{v}_{F,x}^2$ and $\bar{v}_{F,y}^2$ definitely promotes a pronounced anisotropic electronic response and consequently a broad hyperbolic region.

C. Electronic structure and optical conductivity of Pd-S-Cl monolayer

To verify the hyperbolic nature of our TB model, we examine a Pd-S-Cl monolayer sourced from the Computational 2D Materials Database [50]. This monolayer exhibits a rectangular lattice with the layer group of pmmn (no. 46). The optimized lattice constants are respectively $a = 5.20 \text{ \AA}$ and $b = 3.46 \text{ \AA}$, encompassing two Pd, two S, and two Cl atoms within each unit cell. It consists of a buckled Pd-S atomic layer sandwiched by the two outermost Cl atomic layers, as depicted in Fig. 3(a). Within the Pd-S layer, each Pd (or S) atom is fourfold-coordinated by S (or Pd) atoms. Along the y direction, each Cl atom is bonded to two Pd atoms. The stability of the Pd-S-Cl monolayer is verified from the phonon spectrum and molecular dynamics simulations, as depicted in Fig. S1 in the Supplemental Material [51]. Notably, the buckled Pb-S layer bears a resemblance to the lattice structure in our TB model. Notably, similar lattice structure of

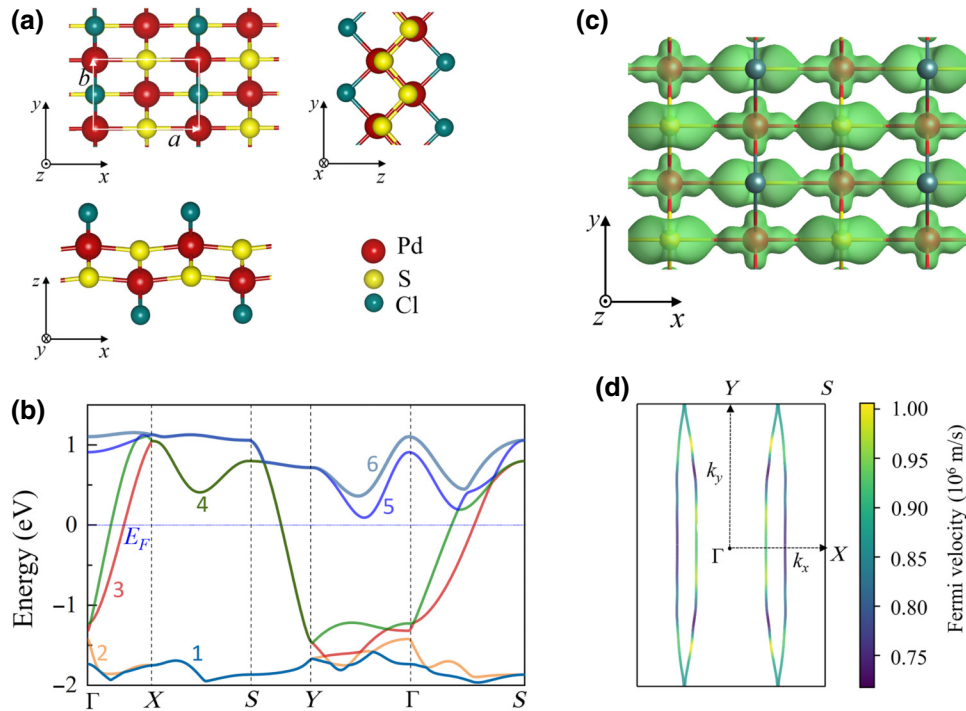


FIG. 3. Lattice and electronic structures of Pd-S-Cl monolayer. (a) Lattice structure of Pd-S-Cl monolayer viewed from [001], [100], and [010] directions. (b) The electronic band structure of Pd-S-Cl monolayer. The energy at the Fermi level is set to zero. (c) The isosurfaces of the charge density for the states at the Fermi level. (d) The contours of the Fermi surface.

2D Cr-S-Br materials has been synthesized and extensively investigated in experiments [52–54].

The electronic structures of the Pd-S-Cl monolayer obtained from DFT calculations are presented in Figs. 3(b)–3(d). The electronic bands in the proximity to the Fermi level, as depicted in Fig. 3(b), exhibit significant anisotropy, with pronounced dispersion along the Γ - X direction and flatter profiles along the Γ - Y direction. Specifically, along the Γ - X direction, two dispersive bands cross the Fermi level, whereas a band gap of about 1.23 eV emerges along the Γ - Y direction, resembling the bands of the TB model. Further analysis indicates that the two dispersive bands (3 and 4) are contributed mainly by the $d_{x^2-y^2}$ orbital of Pd and the p_x orbital of S atoms, as illustrated in Fig. S2 in the Supplemental Material [51], which form a conducting channel along the x direction, as evidenced by the Kohn-Sham electron wave functions, as depicted in Fig. 3(c). The pronounced anisotropy in electronic structure near the Fermi level is also evidenced by the emergence of two slender-olive-like Fermi contours, as illustrated in Fig. 3(d). These findings are well consistent with the TB model. Interestingly, anisotropic electronic properties characterized by a quasi-one-dimensional system have been observed in the van der Waals layered Cr-S-Br semiconductor [52–54]. Our TB model captures the anisotropic electronic band structures of monolayer Cr-S-Br. The semiconducting nature

of Cr-S-Br is attributed to the lower valence electron count of Cr atoms compared with Pd. In particular, the observational evidence highlights the presence of steady-state hyperbolic exciton polaritons in Cr-S-Br, which is attributed to the anisotropic exciton resonances [55].

We then evaluate the optical conductivity tensor of the Pd-S-Cl monolayer using Eq. (5) with both $E_{k,l}$ and $|\mathbf{k}, l\rangle$ being obtained from first-principles calculations. The real and imaginary components of the optical conductivity tensor are separately illustrated in Fig. 4(a). The imaginary component of optical conductivity ($\text{Im } \sigma_{jj}$) signifies a material's response to an electric field, whereas the real component ($\text{Re } \sigma_{jj}$) quantifies the extent of energy dissipation caused by light absorption along the j direction. Within the frequency range of $0.50 < \omega < 2.85$ eV, the Pd-S-Cl monolayer exhibits a hyperbolic feature with $\text{Im } \sigma_{xx} > 0$ and $\text{Im } \sigma_{yy} < 0$, spanning from the near-infrared region to the visible regime. Furthermore, within this hyperbolic region, both $\text{Re } \sigma_{xx}$ and $\text{Re } \sigma_{yy}$ remain small, except for a peak in $\text{Re } \sigma_{xx}$ near 2.6 eV. The small real parts of optical conductivity signify minimal light absorption losses, benefiting the propagation of SPPs in the monolayer. The lattice parameters and hyperbolic properties of MYZ ($M = \text{Co, Pd, Ru, Rh}$; $Y = \text{S, Se, Te}$; and $Z = \text{Cl, Br}$) monolayers are presented in Table S1 in the Supplemental Material [51]. Notably, the optical conductivity spectra, despite their inability to be straightforwardly

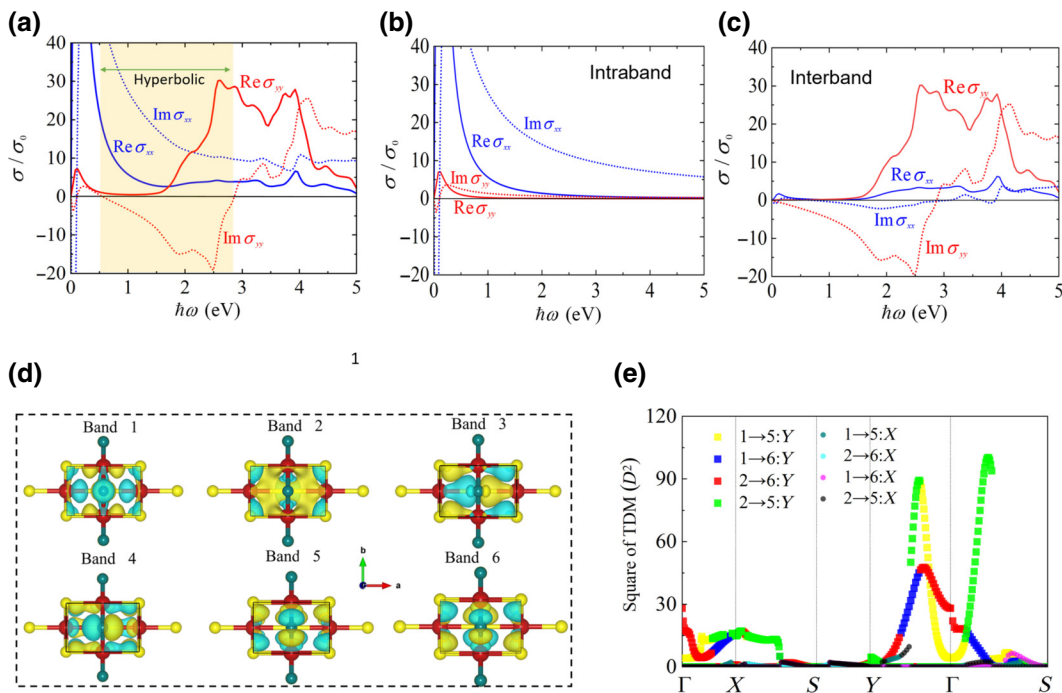


FIG. 4. The relation between conductivity and electronic structures of Pd-S-Cl monolayer. (a) The conductivity of Pd-S-Cl monolayer in units of $\sigma_0 = e^2/16\hbar$. Contributions of (b) intraband transitions and (c) interband transitions. (d) Bloch electron wave functions of the six bands at the Γ point. (e) Squares of the TDMs of the interband transitions along the x and y directions for the six bands identified in (d).

fitted using Eq. (5) due to the multiple peaks resulting from complex interband transitions, exhibit the characteristics outlined in Fig. 1(d). This highlights the distinct contributions of intraband transitions and interband transitions along the x and y directions, a characteristic trait for these 2D hyperbolic materials.

Further insight into the roles of intraband and interband transitions within the optical conductivity tensor is provided in Figs. 4(b) and 4(c). In the context of intraband transitions, $\text{Im} \sigma_{xx}$ manifests significant metallic response characteristics along the x direction, whereas $\text{Im} \sigma_{yy}$ remains negligible, signifying dielectric responses along this direction. These features are well consistent with the anisotropic electronic band structure of the Pd-S-Cl monolayer. In the case of interband transitions, multiple peaks emerge in the $\text{Re} \sigma_{yy}$ spectrum, whereas $\text{Re} \sigma_{xx}$ becomes negligible, as depicted in Fig. 4(c). These peaks verify the substantial contributions of interband transitions to the optical conductivity tensor along the y direction, leading to the reduction of $\text{Im} \sigma_{yy}$ values to negative within a specific frequency region, according to Eq. (5).

The peaks of $\text{Re} \sigma_{yy}$ originate from electron transitions from the fully occupied bands (1 and 2) to the empty bands (5 and 6), as labeled in Fig. 3(b), and

thus are constrained by the symmetries of these bands. Further analysis indicates that the electron wave functions of bands 1 and 2 have even parity in both the x and y directions, whereas those of bands 5 and 6 exhibit even parity along the x direction but odd parity along the y direction, as depicted in Fig. 4(d). Therefore, only $\langle \mathbf{k}, 1 | \hat{v}_y | \mathbf{k}, 5 \rangle$, $\langle \mathbf{k}, 1 | \hat{v}_y | \mathbf{k}, 6 \rangle$, $\langle \mathbf{k}, 2 | \hat{v}_y | \mathbf{k}, 5 \rangle$, and $\langle \mathbf{k}, 2 | \hat{v}_y | \mathbf{k}, 6 \rangle$ have nonzero values, leading to the anisotropic interband transitions in the Pd-S-Cl monolayer. This is also consistent with the direction-dependent squares of the transition dipole moments (TDMs) for the interband transition, as illustrated in Fig. 4(e). For the interband transitions $1 \rightarrow 5$, $1 \rightarrow 6$, $2 \rightarrow 5$, and $2 \rightarrow 6$, the TDMs along the y direction have greater values than along the x direction. These results demonstrate the pronounced contribution of interband transitions to electron optical conductivity along the y direction compared with that along the x direction, resulting in $S_{yy} \gg S_{xx}$. Combining with the different intraband transition contributions along the x and y directions, $D_{xx} \gg D_{yy}$, owing to the slender-olive-like Fermi contours, we have $\omega_{0,y} \ll \omega_{0,x}$, and subsequently a broad hyperbolic region. One should notice that $\text{Im} \sigma_{xx}$ of the Pd-S-Cl monolayer maintains positive values within the frequency region considered in this

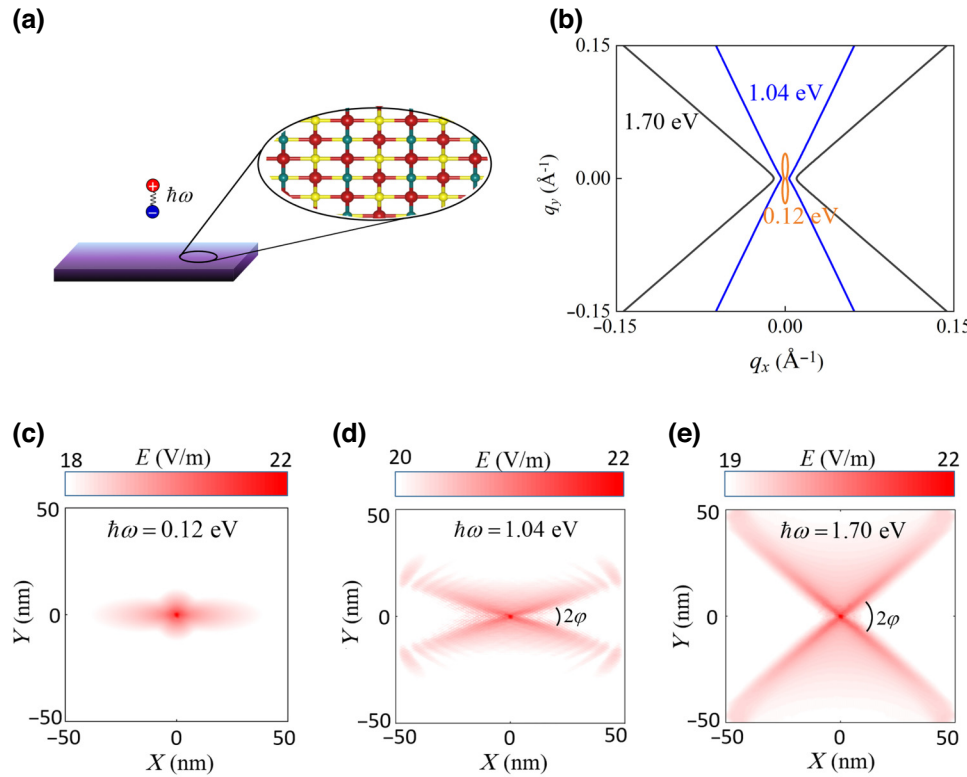


FIG. 5. Surface plasmon polaritons on Pd-S-Cl nanosheet. (a) Schematic representation of the excitation of surface plasmons on a Pd-S-Cl nanosheet using a vertically polarized electric dipole. (b) Isofrequency profiles of the surface plasmons on a Pd-S-Cl nanosheet at frequencies of $\hbar\omega = 0.12$, 1.04 , and 1.70 eV. (c)–(e) The spatial distribution of the electric field (E) for the surface plasmons at different frequencies.

work, owing to the weak interband transition effect along the x direction. The interband transitions contribute to the shift of $\text{Im } \sigma_{yy}$ from negative to positive values, establishing the upper boundary of the hyperbolic region, consistent with the case of Fig. 1(d).

D. Hyperbolic SPPs in Pd-S-Cl monolayer

We conduct numerical simulations to investigate the directional propagation of SPPs in the Pd-S-Cl monolayer. The model consists of a Pd-S-Cl sheet with dimensions of $100 \times 20 \text{ nm}^2$, positioned within a vacuum environment. We employ a z -polarized dipole source located 1 nm above the sheet to excite SPPs, as illustrated in Fig. 5(a). The numerical solution of Maxwell's equations is accomplished using a finite-difference time-domain method [56]. We select three specific frequencies, $\omega = 0.12, 1.04$, and 1.70 eV . The corresponding optical conductivity tensors at these frequencies are obtained from first-principles calculations, which are $\sigma_{xx} = 2.108 \text{ mS} + 0.383i \text{ mS}$ and $\sigma_{yy} = 0.107 \text{ mS} + 0.011i \text{ mS}$, $\sigma_{xx} = 0.0026 \text{ mS} + 0.392i \text{ mS}$ and $\sigma_{yy} = 0.0026 \text{ mS} - 0.0559i \text{ mS}$, and $\sigma_{xx} = 0.00039 \text{ mS} + 0.2217i \text{ mS}$ and $\sigma_{yy} = 0.00037 \text{ mS} - 0.1826i \text{ mS}$, respectively. For the last two frequencies within the hyperbolic region, the IFCs of SPPs exhibit hyperbolic characteristics in the momentum space, as depicted in Fig. 5(b). For $\omega = 0.12 \text{ eV}$, the IFC exhibits a slender dumbbell shape orientating along the y direction, owing to the exceptionally high anisotropy of the conductivities along the x and y directions, $\text{Im } \sigma_{xx} \gg \text{Im } \sigma_{yy}$. These features are in consistent with Eq. (7).

The directional propagation of the SPPs in the Pd-S-Cl sheet can be evidenced by the spatial distribution of electric field obtained by solving Maxwell's equations using the finite-element method, as illustrated in Figs. 5(c)–5(e). For the SPPs at $\omega = 0.12 \text{ eV}$, the electric field is confined within two narrow beams orientating along the x direction. This aligns with the slender dumbbell IFC orientating along the y direction. For $\omega = 1.04$ and 1.70 eV within the hyperbolic region, the electric field is confined within four beams with an angle of $2\varphi = 16.23^\circ$ and 78.95° between them, which are consistent with the theoretical predictions based on $\varphi = \pm \tan^{-1} |\text{Im } \sigma_{yy}/\text{Im } \sigma_{xx}|^{1/2}$. These observations substantiate the directional propagation of SPPs within the Pd-S-Cl monolayer.

E. Hyperbolicity of MYZ monolayers

The Pd-S-Cl monolayer boasts a wealth of analogues, MYZ ($M = \text{Co, Pd, Ru, Rh}$; $Y = \text{S, Se, Te}$; and $Z = \text{Cl, Br, I}$). These analogues share similar lattice structures and exhibit anisotropic electronic band structures along the Γ - X and Γ - Y directions, as depicted in Fig. S3 in the Supplemental Material [51]. Notably, for Pd- Y - Z and Ru- Y - Z monolayers, the electronic band structures near the Fermi level can be effectively described by the TB model.

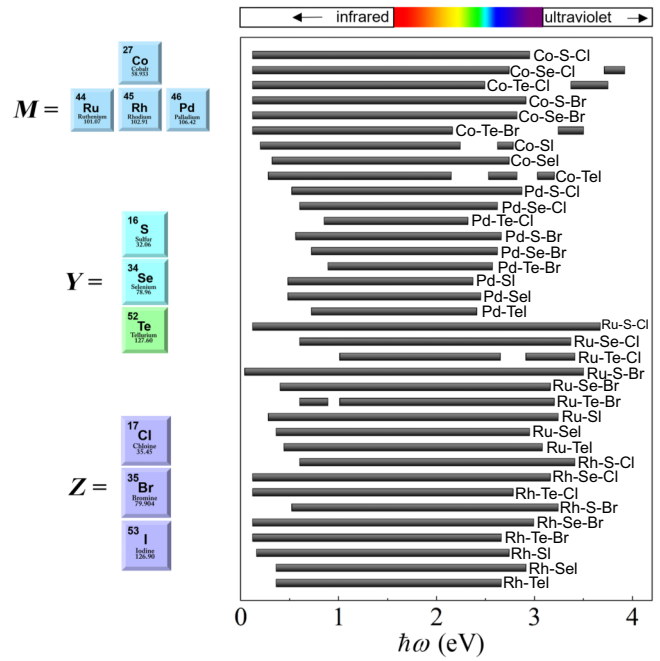


FIG. 6. The hyperbolic regions of MYZ monolayers with $M = \text{Co, Pd, Ru, Rh}$; $Y = \text{S, Se, Te}$; $Z = \text{Cl, Br, I}$ obtained from first-principles calculations.

It is not surprising to observe hyperbolic regions in these analogues, as depicted in Fig. 6 and Fig. S4 in the Supplemental Material [51]. Most of these 2D materials showcase hyperbolic regions that span the entire near-infrared to visible spectrum, underscoring their potential for developing hyperbolic media and device applications. The broad hyperbolic regions identified in these 2D materials validate the design principles of 2D hyperbolic materials proposed in this work, providing a rich pool of candidates for the exploration of 2D hyperbolicity.

Finally, it is important to emphasize the correlations between the Drude weight (D_{jj}) and Fermi velocity (\bar{v}_j^2), and between the hyperbolicity band and the ratios of D_{jj} to S_{jj} as expressed in Eq. (8). These correlations offer an effective strategy for rapidly prescreening 2D materials with broadband hyperbolicity based on their electronic band structures. Specifically, if a 2D material exhibits dispersive bands with high Fermi velocity in one direction and relatively flat bands with low Fermi velocity in an orthogonal direction, it would possess highly anisotropic Drude weights. This would promote the formation of a broad hyperbolic region, assuming S_{jj} exhibits weak or inverse anisotropy, as illustrated in Figs. 1(c) and 1(d). Obviously, this principle is effectively applicable to these MYZ monolayers. Given that the electronic band structures of 2D materials are readily available in numerous material databases, our findings offer a practical method for large-scale screening of 2D hyperbolic materials.

IV. CONCLUSIONS

In summary, our study has demonstrated a definitive relationship between the anisotropic electronic structure and hyperbolic region in 2D NHMs. By introducing the averaged square Fermi velocity as a descriptor for electronic structure anisotropy, which correlates with the Drude weight (D_{jj}) in optical conductivity, we have been able to provide a deeper understanding of 2D NHMs. Our proposed 2D lattice model, composed of p and d orbitals, reveals a pronounced anisotropic electronic structure and a significant hyperbolic nature due to anisotropic orbital ordering. Utilizing this model, we have revealed a series of 2D NHMs, denoted as MYZ ($M = \text{Co, Pd, Ru, Rh}$; $Y = \text{S, Se, Te}$; and $Z = \text{Cl, Br, I}$), which showcase broadband hyperbolicity as confirmed by first-principles calculations. The hyperbolic dispersion in these materials spans from the near-infrared to the visible-light spectrum. Furthermore, we have validated the directional propagation of SPPs on these 2D materials by applying Maxwell's equations. The exceptional hyperbolicity observed in these materials can be ascribed to the highly anisotropic electronic structures, which are a consequence of anisotropic orbital ordering within the lattices. Our research not only elucidates the fundamental mechanisms that govern hyperbolic behavior in 2D materials but also provides a solid foundation for future research and potential applications of 2D NHMs in various technological domains.

ACKNOWLEDGMENTS

This study is supported by the National Natural Science Foundation of China (Grant No. 12074218) Taishan Scholar Program of Shandong Province (Grant No. ts20190906).

- [1] W. L. Barnes, A. Dereux, and T. W. Ebbesen, Surface plasmon subwavelength optics, *Nature* **424**, 824 (2003).
- [2] J. B. Pendry, L. Martín-Moreno, and F. J. García-Vidal, Mimicking surface plasmons with structured surfaces, *Science* **305**, 847 (2004).
- [3] A. A. High, R. C. Devlin, A. Dibos, M. Polking, D. S. Wild, J. Perczel, N. P. de Leon, M. D. Lukin, and H. Park, Visible-frequency hyperbolic metasurface, *Nature* **522**, 192 (2015).
- [4] J. S. Gomez-Diaz, M. Tymchenko, and A. Alù, Hyperbolic plasmons and topological transitions over uniaxial metasurfaces, *Phys. Rev. Lett.* **114**, 233901 (2015).
- [5] T. Xu, A. Agrawal, M. Abashin, K. J. Chau, and H. J. Lezec, All-angle negative refraction and active flat lensing of ultraviolet light, *Nature* **497**, 470 (2013).
- [6] H. Shin and S. Fan, All-angle negative refraction for surface plasmon waves using a metal-dielectric-metal structure, *Phys. Rev. Lett.* **96**, 073907 (2006).
- [7] J. Haug, M. Palei, J. D. Shrout, E. Narimanov, P. W. Bohn, and A. J. Hoffman, Confined hyperbolic metasurface modes for structured illumination microscopy, *Opt. Express* **29**, 42331 (2021).
- [8] Y. U. Lee, S. Li, G. B. M. Wisna, J. Zhao, Y. Zeng, A. R. Tao, and Z. Liu, Hyperbolic material enhanced scattering nanoscopy for label-free super-resolution imaging, *Nat. Commun.* **13**, 6631 (2022).
- [9] J. Lin, J. P. B. Mueller, Q. Wang, G. Yuan, N. Antoniou, X.-C. Yuan, and F. Capasso, Polarization-controlled tunable directional coupling of surface plasmon polaritons, *Science* **340**, 331 (2013).
- [10] B. Liu and S. Shen, Broadband near-field radiative thermal emitter/absorber based on hyperbolic metamaterials: Direct numerical simulation by the Wiener chaos expansion method, *Phys. Rev. B* **87**, 115403 (2013).
- [11] H. Salihoglu and X. Xu, Near-field radiative heat transfer enhancement using natural hyperbolic material, *J. Quant. Spectrosc. Radiat. Transfer* **222**, 115 (2019).
- [12] R. Liu, Z. Zha, M. Shafi, C. Li, W. Yang, S. Xu, M. Liu, and S. Jiang, Bulk plasmon polariton in hyperbolic metamaterials excited by multilayer nanoparticles for surface-enhanced Raman scattering (SERS) sensing, *Nanophotonics* **10**, 2949 (2021).
- [13] Y. Zhao, A. Hubarevich, M. Iarossi, T. Borzda, F. Tantussi, J.-A. Huang, and F. De Angelis, Hyperbolic nanoparticles on substrate with separate optical scattering and absorption resonances: A dual function platform for SERS and thermoplasmonics, *Adv. Opt. Mater.* **9**, 2100888 (2021).
- [14] C. Cheng, W. Chen, Y. Lu, F. Ruan, and G. Li, Large near-field enhancement in terahertz antennas by using hyperbolic metamaterials with hole arrays, *Appl. Sci.* **9**, 2524 (2019).
- [15] O. N. Kozina and L. A. Melnikov, Graphene hyperbolic nanostructure for generation of terahertz wave, *J. Commun. Technol. Electron.* **67**, 1304 (2022).
- [16] F. Wu, G. Lu, Z. Guo, H. Jiang, C. Xue, M. Zheng, C. Chen, G. Du, and H. Chen, Redshift gaps in one-dimensional photonic crystals containing hyperbolic metamaterials, *Phys. Rev. Appl.* **10**, 064022 (2018).
- [17] S. V. Zhukovsky, A. A. Orlov, V. E. Babicheva, A. V. Lavrinenko, and J. E. Sipe, Photonic-band-gap engineering for volume plasmon polaritons in multiscale multilayer hyperbolic metamaterials, *Phys. Rev. A* **90**, 013801 (2014).
- [18] F. Wu, M. Chen, and S. Xiao, Wide-angle polarization selectivity based on anomalous defect mode in photonic crystal containing hyperbolic metamaterials, *Opt. Lett.* **47**, 2153 (2022).
- [19] J. Chen, M. Badioli, P. Alonso-Gonzalez, S. Thongrattanasiri, F. Huth, J. Osmond, M. Spasenovic, A. Centeno, A. Pesquera, P. Godignon, A. Zurutuza Elorza, N. Camara, F. Javier Garcia de Abajo, R. Hillenbrand, and F. H. L. Koppens, Optical nano-imaging of gate-tunable graphene plasmons, *Nature* **487**, 77 (2012).
- [20] Z. Fei, A. S. Rodin, G. O. Andreev, W. Bao, A. S. McLeod, M. Wagner, L. M. Zhang, Z. Zhao, M. Thiemens, G. Dominguez, M. M. Fogler, A. H. Castro Neto, C. N. Lau, F. Keilmann, and D. N. Basov, Gate-tuning of graphene plasmons revealed by infrared nano-imaging, *Nature* **487**, 82 (2012).
- [21] L. Ju, B. Geng, J. Horng, C. Girit, M. Martin, Z. Hao, H. A. Bechtel, X. Liang, A. Zettl, Y. R. Shen, and F. Wang, Graphene plasmonics for tunable terahertz metamaterials, *Nat. Nanotechnol.* **6**, 630 (2011).
- [22] A. N. Grigorenko, M. Polini, and K. S. Novoselov, Graphene plasmonics, *Nat. Photonics* **6**, 749 (2012).

- [23] G. Jia, J. Luo, H. Wang, Q. Ma, Q. Liu, H. Dai, and R. Asgari, Two-dimensional natural hyperbolic materials: From polaritons modulation to applications, *Nanoscale* **14**, 17096 (2022).
- [24] P. N. Li, I. Dolado, F. J. Alfaro-Mozaz, F. Casanova, L. E. Hueso, S. Liu, J. H. Edgar, A. Y. Nikitin, S. Vélez, and R. Hillenbrand, Infrared hyperbolic metasurface based on nanostructured van der Waals materials, *Science* **359**, 892 (2018).
- [25] Z. Zheng, N. Xu, S. L. Oscurato, M. Tamagnone, F. Sun, Y. Jiang, Y. Ke, J. Chen, W. Huang, W. L. Wilson, A. Ambrosio, S. Deng, and H. Chen, A mid-infrared biaxial hyperbolic van der Waals crystal, *Sci. Adv.* **5**, eaav8690 (2019).
- [26] E. Ozbay, Plasmonics: Merging photonics and electronics at nanoscale dimensions, *Science* **311**, 189 (2006).
- [27] D. Rodrigo, O. Limaj, D. Janner, D. Etezadi, F. Javier Garcia de Abajo, V. Pruneri, and H. Altug, Mid-infrared plasmonic biosensing with graphene, *Science* **349**, 165 (2015).
- [28] S. Castilla, I. Vangelidis, V.-V. Pusapati, J. Goldstein, M. Autore, T. Slipchenko, K. Rajendran, S. Kim, K. Watanabe, T. Taniguchi, L. Martin-Moreno, D. Englund, K.-J. Tielrooij, R. Hillenbrand, E. Lidorikis, and F. H. L. Koppens, Plasmonic antenna coupling to hyperbolic phonon-polaritons for sensitive and fast mid-infrared photodetection with graphene, *Nat. Commun.* **11**, 4872 (2020).
- [29] A. Nemilentsau, T. Low, and G. Hanson, Anisotropic 2D materials for tunable hyperbolic plasmonics, *Phys. Rev. Lett.* **116**, 066804 (2016).
- [30] E. van Veen, A. Nemilentsau, A. Kumar, R. Roldan, M. I. Katsnelson, T. Low, and S. Yuan, Tuning two-dimensional hyperbolic plasmons in black phosphorus, *Phys. Rev. Appl.* **12**, 014011 (2019).
- [31] Z. Torbatian, D. Novko, and R. Asgari, Tunable low-loss hyperbolic plasmon polaritons in a T_d -WTe₂ single layer, *Phys. Rev. Appl.* **14**, 044014 (2020).
- [32] C. Wang, S. Huang, Q. Xing, Y. Xie, C. Song, F. Wang, and H. Yan, Van der Waals thin films of WTe₂ for natural hyperbolic plasmonic surfaces, *Nat. Commun.* **11**, 1158 (2020).
- [33] F. L. Ruta, B. S. Y. Kim, Z. Sun, D. J. Rizzo, A. S. McLeod, A. Rajendran, S. Liu, A. J. Millis, J. C. Hone, and D. N. Basov, Surface plasmons induce topological transition in graphene/ α -MoO₃ heterostructures, *Nat. Commun.* **13**, 3719 (2022).
- [34] A. Bapat, S. Dixit, Y. Gupta, T. Low, and A. Kumar, Gate tunable light-matter interaction in natural biaxial hyperbolic van der Waals heterostructures, *Nanophotonics* **11**, 2329 (2022).
- [35] G. Kresse and J. Furthmüller, Electronic structure of two-dimensional crystals from ab initio theory, *Phys. Rev. B* **54**, 11169 (1996).
- [36] J. Enkovaara, *et al.*, Electronic structure calculations with GPAW: A real-space implementation of the projector augmented-wave method, *J. Phys.: Condens. Matter* **22**, 253202 (2010).
- [37] J. Yan, J. J. Mortensen, K. W. Jacobsen, and K. S. Thygesen, Linear density response function in the projector augmented wave method: Applications to solids, surfaces, and interfaces, *Phys. Rev. B* **83**, 245122 (2011).
- [38] P. E. Blöchl, Projector augmented-wave method, *Phys. Rev. B* **50**, 17953 (1994).
- [39] J. P. Perdew, K. Burke, and M. Ernzerhof, Generalized gradient approximation made simple, *Phys. Rev. Lett.* **77**, 3865 (1996).
- [40] G. F. Giuliani and G. Vignale, in *Quantum Theory of the Electron Liquid* (Cambridge University Press, Cambridge, 2005).
- [41] C. Ding, Y. Du, and M. Zhao, Inhomogeneous and nonlocal optical response in magic angle twisted trilayer graphene, *Phys. Rev. B* **109**, 125431 (2024).
- [42] V. P. Gusynin, S. G. Sharapov, and J. P. Carbotte, Unusual microwave response of Dirac quasiparticles in graphene, *Phys. Rev. Lett.* **96**, 256802 (2006).
- [43] S. A. Mikhailov and K. Ziegler, New electromagnetic mode in graphene, *Phys. Rev. Lett.* **99**, 016803 (2007).
- [44] J. F. Wang, X. L. Sui, W. H. Duan, F. Liu, and B. Huang, Density-independent plasmons for terahertz-stable topological metamaterials, *Proc. Natl. Acad. Sci. U. S. A.* **118**, 19 (2021).
- [45] C. Ding, X. Zhang, H. Gao, X. Ma, Y. Li, and M. Zhao, Role of electron-electron interaction in the plasmon modes of twisted bilayer graphene, *Phys. Rev. B* **106**, 15 (2022).
- [46] H. Gao, X. Zhang, C. Ding, X. Ma, M. Wang, Y. Li, and M. Zhao, Highly directional and carrier density-independent plasmons in quasi-one-dimensional electron gas systems, *Commun. Phys.* **6**, 342 (2023).
- [47] D. N. Basov, M. M. Fogler, and F. J. Garcia de Abajo, Polaritons in van der Waals materials, *Science* **354**, aag1992 (2016).
- [48] G. W. Hanson, Dyadic Green's functions for an anisotropic, non-local model of biased graphene, *IEEE Trans. Antennas Propag.* **56**, 747 (2008).
- [49] J. C. Slater and G. F. Koster, Simplified LCAO method for the periodic potential problem, *Phys. Rev.* **94**, 1498 (1954).
- [50] M. N. Gjerding, A. Taghizadeh, A. Rasmussen, S. Ali, F. Bertoldo, T. Deilmann, N. R. Knosgaard, M. Kruse, A. H. Larsen, S. Manti, T. G. Pedersen, U. Petralanda, T. Skovhus, M. K. Svendsen, J. J. Mortensen, T. Olsen, and K. S. Thygesen, Recent progress of the computational 2D materials database (C2DB), *2D Mater.* **8**, 044002 (2021).
- [51] See Supplemental Material <http://link.aps.org/supplemental/10.1103/PhysRevApplied.22.024005> for the stability, lattice and electronic structures, and conductivities of MYZ ($M = \text{Co, Pd, Ru, Rh}$; $Y = \text{S, Se, Te}$; and $Z = \text{Cl, Br, I}$) monolayers.
- [52] J. Klein, *et al.*, The bulk van der Waals layered magnet CrSBr is a quasi-1D material, *ACS Nano* **17**, 5316 (2023).
- [53] F. Wu, I. Gutierrez-Lezama, S. A. Lopez-Paz, M. Gibertini, K. Watanabe, T. Taniguchi, F. O. von Rohr, N. Ubrig, and A. F. Morpurgo, Quasi-1D electronic transport in a 2D magnetic semiconductor, *Adv. Mater.* **34**, 2109759 (2022).
- [54] N. P. Wilson, K. Lee, J. Cenker, K. Xie, A. H. Dismukes, E. J. Telford, J. Fonseca, S. Sivakumar, C. Dean, T. Cao, X. Roy, X. Xu, and X. Zhu, Interlayer electronic coupling on demand in a 2D magnetic semiconductor, *Nat. Mater.* **20**, 1657 (2021).
- [55] F. L. Ruta, *et al.*, Hyperbolic exciton polaritons in a van der Waals magnet, *Nat. Commun.* **14**, 8261 (2023).
- [56] K. S. Yee, Numerical solution of initial boundary value problems involving Maxwell's equations in isotropic media, *IEEE Trans. Antennas Propag.* **14**, 302 (1966).